Journal of Power Sources 195 (2010) 4842–4852

Contents lists available at ScienceDirect

Journal of Power Sources

journal homepage: www.elsevier.com/locate/jpowsour

A study of multi-phase flow through the cathode side of an interdigitated flow field using a multi-fluid model

Torsten Berning*, Madeleine Odgaard, Søren Knudsen Kær

Department of Energy Technology, Aalborg University, Pontoppidanstraede 101, 9220 Aalborg, Denmark

ARTICLE INFO

Article history:
Received 31 October 2009
Received in revised form 14 January 2010
Accepted 8 February 2010
Available online 13 February 2010

Keywords:
Polymer electrolyte membrane fuel cells
Fuel cell modeling
Multi-phase flow
Multi-fluid model
CFD modeling

ABSTRACT

This work presents a study of multi-phase flow through the cathode side of a polymer electrolyte membrane fuel cell employing an interdigitated flow field plate. A previously published model has been extended in order to account for phase change kinetics, and a comparison between the interdigitated flow field design and a conventional straight channel design has been conducted. It is found that the parasitic pressure drop in the interdigitated design is in the range of a few thousand Pa and could be reduced to a few hundred Pa by choosing diffusion media with high in-plane permeability. The additional compressor work due to the increased pressure loss will only slightly increase, and this may be offset by operating at lower stoichiometries as the interdigitated design is less mass transfer controlled, which means that the overall efficiency of the interdigitated arrangement will be higher. In the interdigitated design more product water is carried out of the cell in the vapor phase compared to the straight channel design which indicates that liquid water management might be less problematic. This effect also leads to the finding that in the interdigitated design more waste heat is carried out of the cell in the form of latent heat which reduces the load on the coolant. Finally we see that the micro-porous layer might help keep the gas diffusion layer substrate dry due to a potentially higher evaporation rate caused by a combination of the Kelvin effect and a larger specific surface area compared to the diffusion layer substrate.

1. Introduction

One general major question of fuel cell design concerns the detailed geometry of the flow field plates. The different possible designs include straight, parallel channels which have a small pressure drop and gas velocities, serpentine channels which have a larger pressure drop and higher gas velocities, or the interdigitated design where straight inlet channels are dead-ended and a convective flow of the gas and liquid is enforced through the porous gas "diffusion" media (GDM) to the straight outlet channels at the cost of an increased pressure drop. This paper describes a numerical study that compares the interdigitated cell design with straight channel cell design employing a newly developed computational model that is based on the formerly commercial software code CFX-4.4. The model employs the so-called multi-fluid approach, which solves one complete set of transport equations for each phase. The physics of phase change have now been implemented and the model also accounts for the Kelvin effect. Other details of the model have been described in a previous publication [1]. In brief, the model allows for the specification of material parameters such as the irreducible saturation, the in- and through-plane permeability, porosity and average contact angle of the liquid phase in every porous layer, i.e. catalyst layer (CL), micro-porous layer (MPL) and gas diffusion layer (GDL).

The structure of this paper is as follows: first a description of the model is given and the equations that account for phase change effects are listed in detail. Then a standard case of the interdigitated cell design is investigated, highlighting the different physical effects and showing detailed distributions of important properties such as predicted liquid saturation, relative humidity distribution, oxygen distribution and gas and liquid phase pressure distribution. A detailed study then compares the interdigitated channel design with the parallel channel design under specified operating conditions with varying stoichiometric flow ratio. Advantages of the interdigitated design include a possibility to operate at lower stoichiometric flow ratio, a higher concentration of oxygen inside the catalyst layer, a lesser amount of product water leaving the cell in the liquid phase and a lower and more stable load on the coolant. Next a second case will be investigated in detail where more realistic material parameters are employed than in the first case (irreducible saturation, in- and through-plane permeability, porosity) and it is found that the micro-porous layer may help keeping the gas diffusion layer substrate dryer by enforcing a higher evaporation rate. Finally the Conclusions section will summarize the main findings of this study.

* Corresponding author. Tel.: +45 9940 9261; fax: +45 98151411.
E-mail addresses: tbe@iet.aau.dk, torsten.berning@alumni.uvic.ca (T. Berning), skk@iet.aau.dk (S.K. Kær).

0378-7753/$ – see front matter © 2010 Elsevier B.V. All rights reserved.
doi:10.1016/j.jpowsour.2010.02.017

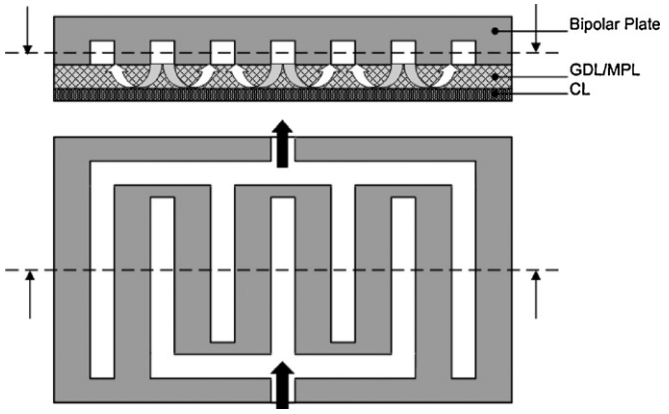

Fig. 1. Schematic of the cathode side with an interdigitated flow field design.

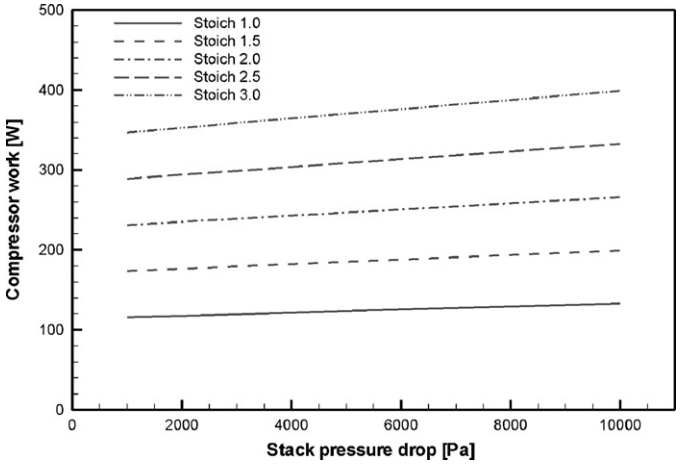

Fig. 2. Compressor work for a stack power of 5 kW and an operating (back-) pressure of 1.5 atm (152 kPa) as function of the stoichiometric flow rate and cell pressure drop. The assumed efficiency of the compressor is 85%.

2. Interdigitated flow field

The interdigitated flow field design was first devised by Nguyen [2] with the goal of reducing the amount of liquid water flooding inside the porous gas diffusion layers of the fuel cell during operation and enhance the oxygen concentration at the catalyst layers by means of forced convection. While it was shown that this flow field design afforded higher limiting current densities one obvious disadvantage of this design is the increased pressure drop due to the forced convection through the porous layers. Modeling and experimental work on interdigitated flow fields was reported in references [3–11]. Fig. 1 shows a schematic of the cathode side of a fuel cell employing an interdigitated flow field plate.

The reported stack pressure drop in the original publication was in the range of 1.4–2.4 kPa for a 1 mm land width depending on the operating conditions [2]. Clearly this pressure drop is a strong function of the overall mass flow (current density) through the porous layer and, more importantly, on the level of liquid saturation. If the air is forced through a highly saturated porous medium the pressure drop increases drastically. To give an example about the importance of the pressure drop in a fuel cell during operation consider this:

Imagine we want to operate a 5 kW fuel cell unit at a stack pressure of 1.5 atm which was previously found to be advantageous with regard to cell power density and limiting current density [12]. The work required to isothermally power the compressor at ambient temperature is given by [13]:

$$W_{\text{compr}} = 1004\ \text{J kg K}^{-1}\ \frac{293\,\text{K}}{\zeta_{\text{compr}}}\left[\left(\frac{1.5\,\text{atm}}{1.0\,\text{atm}}\right)^{0.286} - 1\right]\dot{m} \tag{1}$$

where ζ_{compr} is the efficiency of the compressor and $\dot{m}$ is the mass flow through the compressor. If the maximum power density is taken to be $1\,\text{W cm}^{-2}$ a total cell area of $5000\,\text{cm}^2$ would be required. Typically the maximum power density is achieved in the vicinity of the limiting current density, which we take around $1.5\,\text{A cm}^{-2}$. This means that at this operating point a total current of 7500 A is generated. The amount of oxygen required is:

$$\dot{n}_{O_2} = \frac{7500\ \text{A}}{4(\text{mole-e}^-)(\text{mole-O}_2) \times 96,487\,\text{C/mole-e}^-} \approx 0.02\,\text{mole-O}_2\,\text{s}^{-1} \tag{2}$$

Hence a total of $0.09\,\text{mole s}^{-1}$ dry air has to be compressed. The molar mass of air is $28.84\,\text{g mole}^{-1}$ which results in an overall mass flow of $2.67\,\text{g s}^{-1}$. Assuming a compressor efficiency of 85% the compressor work amounts to 113.6 W or 2.27% of the rated stack output. This however would only hold true for a stoichiometric flow ratio of unity. Typically a stoichiometry of 2 is applied at minimum at the cathode to reduce mass transport losses, which increases the parasitic power required for the compressor to 4.5% of the rated stack power. Due to its effective gas transport the interdigitated design may allow for operation at lower stoichiometric flow ratio of, say, 1.5 and thus increase the overall system efficiency, provided the added pressure drop due to the forced convection over land is not too high. Fig. 2 shows that the advantage of operating at a smaller stoichiometric flow ratio at the cathode side clearly outweighs the disadvantage of having a larger pressure drop across the cell due to the interdigitated plate design.

In addition to the potential for low stoichiometry operation there is the added advantage of having a higher oxygen concentration inside the catalyst layer, as we will see below, which reduces the activation overpotential. We will also see that the claim that the forced convective gas flow provides more effective liquid water removal from the electrodes is warranted only to a limited degree; the main mechanism of liquid water removal is phase change.

3. Model description

3.1. General approach

The model presented here is based on the multi-fluid approach, which means that in contrast to the homogeneous approach [14] and the multi-phase mixture approach [15–17] we are solving for each phase one complete set of transport equations, i.e. continuity equation, momentum equation, energy equation and species equation [18–20]. The detailed mathematical equations are outlined in Berning et al. [1]. The multi-fluid approach utilizes the generic advection-diffusion equation:

$$\nabla \cdot \varepsilon\left(s_\alpha\left(\rho_\alpha U_\alpha \phi_\alpha - \Gamma_\alpha \nabla \phi_\alpha\right)\right) = \varepsilon s_\alpha S_\alpha \tag{3}$$

where s_α denotes the saturation of phase α, ρ is its density, ε is the porosity of a porous medium (for the channel $\varepsilon = 1.0$), U is the velocity vector and ϕ is the transported quantity, e.g. a mass fraction. Γ denotes the molecular diffusion coefficient, i.e. $\Gamma_{A\alpha} = \rho_\alpha D_{A\alpha}$, where $D_{A\alpha}$ is the binary diffusion coefficient of component A in the background fluid of phase α. Note that in case of the momentum equations Γ_α is the dynamic viscosity μ_α of phase α. The term on the right hand side denotes a source term, e.g. through electrochemical reaction or phase change. In case of the momentum equations the source terms are replaced by so-called body force terms which may represent a porous resistance.

The equations solved in the current model are:

- Continuity equations for gas and liquid phase.
- Three-dimensional momentum equations for gas and liquid phase.
- Energy equations for gas and liquid phase.
- Species equations for oxygen and water vapour for the gas and liquid phase.

It should be noted that while two energy equations are currently being solved yielding two temperature fields (gas and liquid) we are inherently assuming that the gas phase, the liquid phase and the solid matrix of the porous media share the same temperature field. Hence we are only interested in a single temperature field, the one of the gas phase where we implement the sink and source terms due to phase change. The liquid phase energy equation is solved but no attention is paid. The same holds true for the species transport equations in the liquid phase, i.e. we could solve for the oxygen concentration in the liquid phase but we pay no attention here. Consequently "zero" equations are being solved for those properties. In a multi-fluid model every transported property is solved for in every thermodynamic phase, which means that we pay a numerical penalty compared to the multi-phase mixture model, where only one set of transport equation is solved [21]. This however is made up by the fact that the multi-fluid model is more physical and numerically simpler to solve.

In case of the gas momentum equation inside a porous medium the generic advection-diffusion equation becomes:

$$\nabla \cdot \varepsilon(s_g(\rho_g U_g \otimes U_g - \mu_g(\nabla U_g + (\nabla U_g)^T))) = \varepsilon s_g \left(\frac{\mu_g}{\varepsilon k_{rel} K} U_g - \nabla p_g\right) \quad (4)$$

where k_{rel} is the relative permeability of the gas phase and p_g is the pressure in the gas phase. It can be seen that if the left hand side of Eq. (4) is negligible (i.e. if the velocities are small) the right hand side reduces to Darcy's law formulated with the intrinsic velocity.

The relative permeability of the gas phase depends on the liquid saturation in the following form:

$$k_{rel,g} = (1 - s)^q \quad (5)$$

where s is the absolute liquid saturation (in contrast to the reducible saturation). The exponent q is difficult to measure and it is frequently assumed to be 3.0. The predicted overall gas phase pressure drop will be very sensitive to this parameter.

The momentum equation for the liquid phase is [1,20]:

$$\nabla \cdot \varepsilon(s_l(\rho_l U_l \otimes U_l - \mu_l(\nabla U_l + (\nabla U_l)^T))) = \varepsilon s_l \left(\nabla p_{cap} + \frac{\mu_l}{\varepsilon k_{rel} K} U_l - \nabla p_g\right) \quad (6)$$

In above equation the capillary pressure p_{cap} and the gas phase pressure p_g may be summarized to the liquid phase pressure according to the definition:

$$p_{cap} = p_g - p_l \quad (7)$$

Hence Eq. (6) can be reduced to Darcy's law in a similar fashion as the gas phase momentum equations.

3.2. Implementation of phase change

Similar to a previous publication by Berning and Djilali [18] the current model requires the specification of phase change kinetics. This is in contrast to the multi-phase mixture model [22], where local equilibrium between the gas phase and the liquid phase is inherently assumed, which means that liquid water cannot co-exist with gas phase at less than 100% relative humidity (RH). The multi-fluid model allows for such condition, which afforded us to study the theoretical propagation of the liquid product water through the porous layers of a fuel cell and identify critical material parameters [1]. That study was conducted in the absence of phase change which means that all the product water corresponding to a certain current density left the cell in the liquid phase. For the current study focusing on the interdigitated cell design we implemented phase change kinetics in the following form:

3.2.1. Evaporation

If there is liquid water in the presence of non-saturated (RH < 100%) gas phase evaporation will occur. The amount of water that evaporates depends on the level of undersaturation and the surface area of the liquid phase. In order to estimate the surface area of the liquid phase it was assumed that it exists in the form of droplets inside the porous media [23,24]. The size of these droplets is assumed to correspond to the pore volume which is estimated from the characteristic pore radius in this work:

$$r_{char} = \sqrt{\frac{K}{\varepsilon}} \quad (8)$$

where K is the dry permeability of the porous medium and ε is its porosity. The overall rate of evaporation of a single droplet is governed by diffusion and convection of water vapour away from the saturated gas–liquid interface into the undersaturated bulk flow according to [25]:

$$\dot{m}_{H_2O,evap} = k_{xm} \pi D^2 M_{H_2O} \frac{x_{A0} - x_{A\infty}}{1 - x_{A0}} \quad (9)$$

where k_{xm} is the convective mass transfer coefficient in [kmol m^{-2} s^{-1}], D is the droplet diameter estimated from the characteristic pore radius, M_{H_2O} is the molecular weight of water, x_{A0} is the molar fraction of water vapor at the gas–liquid interface which corresponds to $p_{sat}(T)/p_{gas}$ and $x_{A\infty}$ is the relative humidity in the bulk flow which corresponds to the molar fraction of water vapour. This in turn can be converted from the mass fraction of water vapour calculated by the CFD solver (note that the mass fraction of water is a transported property, i.e. it is a solution of a transport equation solved by CFD). Eq. (9) stems from the analogy between heat and mass transfer.

The saturation pressure as function of temperature has been approximated:

$$p_{sat}(T) = 2.3865 \times 10^{-1} \times T^3 - 2.2015 \times 10^2 \times T^2 + 6.8113 \times 10^4 \times T - 7.0624 \times 10^6 \quad (10)$$

where p_{sat} is in Pa and T is in Kelvin. This equation is a very good curve-fit of the fundamentally derived exponential expression used by Springer et al. [26] in the temperature range between 40 °C and 100 °C, and it leads to an improved numerical robustness of our code. We can now correct the saturation pressure according to the Kelvin equation [27]:

$$p_{sat,\,corr}(T) = p_{sat}(T) \exp\left(-2\sigma \cos\theta \frac{M_{H_2O}}{\rho_{H_2O,l}} \frac{1}{RT} \left(\frac{\varepsilon}{K}\right)^{0.5}\right) \quad (11)$$

Here σ is the surface tension (0.0625 N m^{-1}), θ is the contact angle, M_{H_2O} is the molecular weight of water, ρ its density, R the universal gas constant and T the local temperature. The characteristic pore dimension is again specified by the porosity ε and permeability K of the porous medium.

The mean convective mass transfer coefficient k_{xm} is calculated according to:

$$k_{xm} = \frac{c D_{H_2O\text{-air}}}{D} Sh_m \quad (12)$$

where c is the total concentration which can be calculated from the ideal gas law, D is again the droplet diameter, $D_{H_2O\text{-air}}$ is the diffusion coefficient of water vapour in air [28]:

$$D_{H_2O\text{-air}} = 1.87 \times 10^{-10} \frac{T^{2.072}}{P} \quad (13)$$

in ($m^2\,s^{-1}$), which applies for a temperature range between 280 K and 450 K. For forced convection around spheres the Sherwood number can be calculated from [25]:

$$Sh_m = 2 + 0.60 Re^{1/2} Sc^{1/3} \quad (14)$$

This again stems from the analogy between heat and mass transfer and it holds for small net mass transfer rates in a flowing fluid approaching with a uniform velocity v_∞ (see below). In our case Eq. (14) should suffice to yield an approximate mass transfer rate. Re is the characteristic Reynolds number:

$$Re = \frac{D v_\infty \rho}{\mu} \quad (15)$$

with D as the droplet diameter, v_∞ is the free-stream velocity, i.e. the calculated speed of the gas phase in the control volume, ρ is the gas phase density and μ is the gas phase dynamic viscosity. It can be seen that for low velocities the Sherwood number reduces to 2. However, at the channel/GDL interface and in case of convection through the porous media as occurs in the interdigitated design there will be a significant convective contribution to the overall mass transfer. The Schmidt number Sc in above equation is calculated according to:

$$Sc = \frac{\mu}{\rho D_{H_2O\text{-air}}} \quad (16)$$

Thus we can calculate the evaporation rate for a single droplet of specified diameter D. The number of droplets then depends on the calculated liquid saturation in every control volume CV of our numerical grid according to [23]:

$$n_{Droplet,CV} = s \frac{V_{CV}}{1/6 \pi D^3} \quad (17)$$

Multiplying the calculated number of droplets in every control volume with the rate of water evaporation per droplet as calculated by Eq. (9) will yield the total amount of water undergoing phase change, and this is implemented as sink and source term for the continuity equations of the liquid phase and the gas phase as well as the species equation of water vapour.

3.2.2. Condensation

Condensation occurs when the local water pressure p_{g,H_2O} exceeds the local saturation pressure $p_{sat}(T)$, and it is fundamentally different from evaporation as it can occur on any hydrophilic surface [24] while evaporation naturally requires the presence of liquid water. In the current model the approach used by Nam and Kaviany was adopted [24], which describes the rate of condensation per unit of interfacial area according to:

$$\dot{m}''_{H_2O,cond} = \frac{1}{4} \bar{u}_m \alpha_m M_{H_2O} \frac{p_{g,H_2O} - p_{H_2O}(T)}{R_g T} \quad (18)$$

where $\bar{u}_m$ is the mean molecular speed $(8 R_g T/\pi M)^{1/2}$ and α_m is the mass accommodation coefficient, taken to be 0.04 [24]. Similar to evaporation, condensation is diffusion controlled, and this is accounted for by an uptake coefficient Γ according to [24]:

$$\frac{1}{\Gamma} = \frac{1}{\alpha_m} + \frac{\bar{u}_m l_D}{4 D_{H_2O\text{-air}}} = \frac{1}{\alpha_m} + \frac{3}{4} \frac{1}{Kn} \quad (19)$$

where D is the characteristic length for diffusion (e.g. pore size) and Kn is the Knudsen number defined as λ/l_D where λ is the mean free path of water vapor. In this work an overall uptake coefficient of $\Gamma = 0.006$ was assumed [24].

In order to calculate the volumetric condensation rate an expression for the interfacial contact area per unit volume A_{lg}/V is needed.

$$\dot{m}'''_{H_2O,cond} = \dot{m}''_{H_2O,cond} \frac{A_{lg}}{V} \quad (20)$$

Similar to the work by Nam and Kaviany a value of 1000 m^{-1} is assumed in this work [24]. Hence the volumetric condensation rate $\dot{m}'''_{H_2O,cond}$ can be obtained, and by multiplying this value with the volume of a control volume CV we obtain the required source and sink term for the liquid phase and gas phase continuity equations as well as the species equation for water vapor for every given control volume in [$kg\,s^{-1}$].

Overall both the evaporation rate and the condensation rate can only be estimated in our current model. We will see in the results section that the calculated relative humidity is close to 100% throughout the two-phase domain indicating "fast" phase change kinetics. A detailed study on the effect of the kinetic parameters on the predicted liquid water distribution and the overall water balance will be conducted in the future.

3.2.3. Latent heat

Eqs. (9)–(17) yield the amount of water evaporated in every given control volume in [$kg\,s^{-1}$] in case of evaporation whereas Eqs. (20)–(22) yield an expression for the amount of mass undergoing phase change in every control volume in case of condensation in [$kg\,s^{-1}$]. Evaporation means we have a source term for the water vapour equation and the gas phase continuity equation as well as a sink term for the liquid phase continuity equation. We also need to correct the energy equation with a source or sink term. The heat of evaporation can be calculated as:

$$r = T \Delta S_r \quad (21)$$

where ΔS_r is the change in entropy due to phase change in [$J\,mol^{-1}\,K^{-1}$]. The heat of evaporation of water can be approximated by a linear function in the temperature range in question [29]:

$$r = 57,555.684\,J\,mol^{-1} - 45.36\,J\,mol^{-1}\,K^{-1} \times T \quad (22)$$

Multiplying Eq. (22) with the amount of water undergoing phase change in every given control volume in [$kg\,s^{-1}$] and dividing by the molecular weight of water in [$kg\,mole^{-1}$] yields the source and sink term for the energy equation for every given control volume in [W].

Note that it is currently assumed that the product water is in the liquid phase. This means for the energy equation that we will have a source term due to reversible and irreversible heating inside the catalyst layer. The source term as proposed by Lampinen and Fomino has been implemented in the current model [30]:

$$q = \left[\frac{T \Delta S}{nF} + \eta_{act} \right] i \quad (23)$$

where i is the local volumetric current density T is the local temperature n is the number of electrons transferred, ΔS is the entropy production, F is Faraday's constant (96,487 C $mole^{-1}$) and η_{act} is the activation overpotential where in this work a constant value of 300 mV has been assumed.

Both the entropy change and the number of electrons n depend on how the cathode half-cell reaction is formulated. For the following notation:

$$O_2 + 4H^+ + 4e^- \rightarrow 2H_2O \quad (24)$$

We have $n = 4$ and $\Delta S_{Pt} = -326.36\,J\,mol^{-1}\,K^{-1}$ [30].

Table 1
Base case material properties.

Parameter	Symbol	Unit	CL	MPL	GDL
Porosity	ε	–	0.75	0.75	0.75
In-plane permeability	$K_{\|\|}$	m^2	1.0×10^{-12}	1.0×10^{-12}	1.0×10^{-12}
Through-plane permeability	$K_{\perp}$	m^2	1.0×10^{-12}	1.0×10^{-12}	1.0×10^{-12}
Contact angle	θ	°	120	120	120
Irreducible saturation	s_{irr}	–	0	0	0

In our current model the local volumetric current density is calculated out of the oxygen concentration according to:

$$i_{local} = i_{avg} \left(\frac{c_{O_2,local}}{c_{O_2,avg}} \right)^{\chi} \quad (25)$$

Where i_{avg} is the pre-specified average current density that the cell operates at, $c_{O2,\,local}$ is the local oxygen concentration in every control volume and $c_{O2,\,avg}$ is the volume-averaged oxygen concentration inside the catalyst layer calculated in the previous iteration. The exponent χ can be freely specified in the current model. In the current simulations a value of unity was applied indicating a strong dependency of the local oxygen concentration on the local current density.

3.3. Boundary and interface conditions

For these simulations a single repeat unit was chosen so that symmetry boundary conditions were applied at both lateral interfaces (z-direction). In the through-plane (y-) direction a temperature boundary condition was applied at the bipolar plate interface, which was the desired cell temperature. This allows heat flux out of the computational domain across this interface which is an integral part of the energy balance conducted below. As this is a solid plate there is no need to specify any boundary condition for the gas phase. The other boundary is located at the catalyst layer where the interface to the membrane would be located. There are no-flux conditions imposed to the gas and liquid phase as well as to the energy equation, meaning that all the waste heat is either picked up by the gas stream (or goes into latent heat) or leaves the cell through the bipolar plate interface where the coolant would be located.

One important boundary condition is applied for the liquid water at the interface between the flow channel and the gas diffusion medium. In this model the liquid phase pressure at the interface is specified as function of the velocity of water coming out of the GDL similar to the well-known Hagen–Poisseuille equation. The number of active sites per unit area is used to scale the velocity, and a good guess is in the range of 1,000,000 active sites per m^2 [31]. The equation for the liquid phase boundary condition is thus [1]:

$$p_{l,int} = p_{l,1} - V_{pore} \left(8\mu_l \frac{\varepsilon}{K} \right) (y_{int} - y_1) \quad (26)$$

where $p_{l,1}$ is the liquid pressure in the first interior cell adjacent to the boundary and y_1 its y-coordinate, while $p_{l,int}$ and y_{int} are the corresponding values at the channel/GDL interface. This expression also incorporates the material porosity ε and permeability K as well as the liquid phase viscosity μ_l. This way the liquid phase pressure at the interface is smaller than in the interior (note that in a hydrophobic medium the liquid pressure is larger than the gas phase pressure). The pore velocity is calculated from the CFD solution according to [1]:

$$V_{pore} = \frac{V_l}{A_y^{CV}} \frac{A}{n_{act}} \quad (27)$$

Where V_l is the y-component of the calculated liquid phase velocity and A_y^{CV} is the y-area of the control volume.

4. Results

The results section consists of the presentation of the base case and highlighting the physics of the interdigitated design. Next a parametrical study will compare the interdigitated design with a conventional straight channel set-up and finally we demonstrate the capabilities of the model by specifying more realistic material conditions in the various layers of the cell.

4.1. Base case simulations

In order to demonstrate the capabilities of the current model base case simulations were conducted. The conditions were chosen at a stoichiometric flow ratio of 2, an inlet RH of 75%, a cell temperature of 80 °C and an outlet pressure of 1.5 atm. Under such conditions there will be a defined evaporation front inside the porous medium. The material parameters used are listed in Table 1. The land and channel width of the cell was 1 mm, the GDL thickness 220 μm, the MPL thickness 30 μm and the CL thickness 10 μm. The computational domain and the numerical grid are shown in Fig. 3. It can be seen that the active area is only 1 mm long (x-direction). Hence the case investigated here can be termed quasi two-dimensional. All two-dimensional (y–z) plots shown in the results section are taken from the middle of the active area.

In the following we want to consider the detailed results for a current density of 1.0 A cm^{-2}. Fig. 4 shows the calculated gas phase pressure drop in a two-dimensional cut. The results from the simulations have been mirrored in the postprocessor for better visualization. The gas enters from the center region and streams to the sides as is indicated by the flow vectors. The predicted pressure drop in this case is close to 2000 Pa, but this value depends strongly on the dry permeability of the diffusion medium, the relative per-

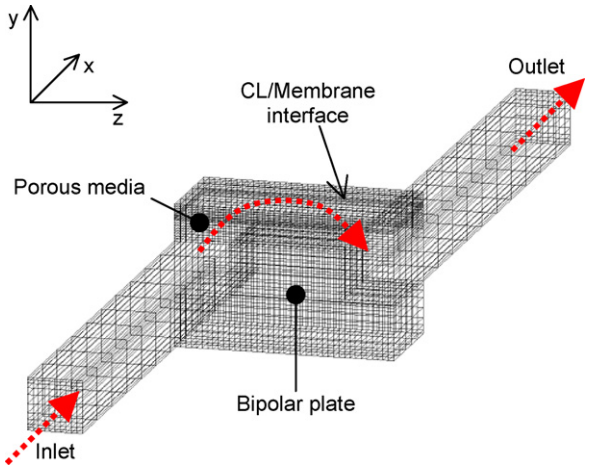

Fig. 3. Numerical grid used for the interdigitated simulations. The inlet is on the lower left and the exit on the upper right. The porous media are the refined section over the channels. The red dotted lines indicate the flow direction.

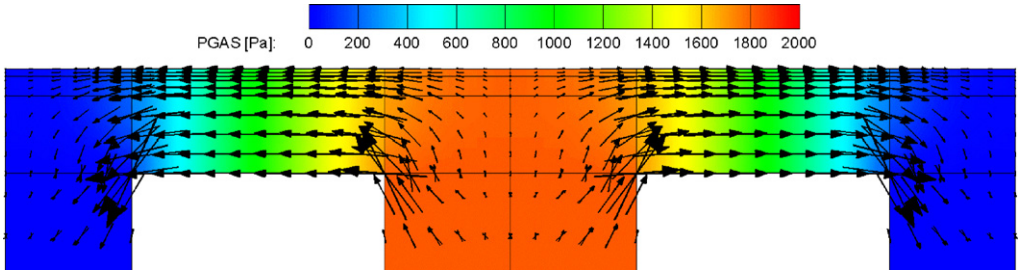

Fig. 4. Predicted gas phase pressure distribution and corresponding flow vectors for the base case investigated. The results have been mirrored and the inlet is in the center. The pressure values are relative to the "reference pressure", i.e. the pressure at the outlet.

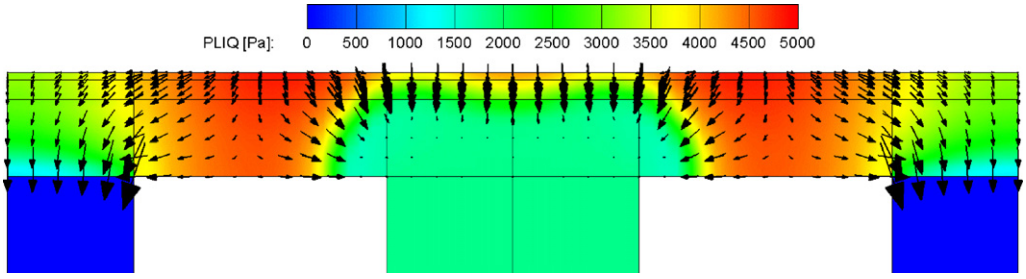

Fig. 5. Predicted liquid phase pressure distribution and corresponding flow vectors for the base case investigated.

meability of the gas phase and the liquid saturation level inside the porous media. A pressure drop of 2000 Pa is in the vicinity of experimentally observed pressure drop [2], and according to Fig. 2 this is a relatively small price to pay in terms of added compression power. Note that despite the fact that the domain investigated here is quasi two-dimensional the pressure drop across the porous medium calculated here is representative for the pressure drop in a three-dimensional set-up when the along-the-channel pressure drop can be neglected.

The calculated liquid phase pressure and the resulting liquid phase flow vectors are shown in Fig. 5. The liquid phase pressure has been calculated out of the difference between the gas phase pressure and the capillary pressure, which depends in turn on the liquid saturation. So in the dry regions the liquid phase pressure becomes identical to the gas phase pressure. It can be seen that the liquid water flows from under the land region towards both the entry and exit channel region. If it were to reach the entry region it would get stuck in the channel section because it cannot enter the hydrophobic GDL. In such cases no steady state solution could be obtained with the model, and accordingly experiments with an interdigitated flow field have to be conducted in a way that the liquid product water cannot enter the dead-ended inlet section. Simulations conducted with this model indicate that the drag between the gas phase and the liquid phase is not sufficient to keep the liquid water from penetrating the channel section (not shown); it has to be accomplished via phase change, which means that conducting experiments where the gas phase is fully saturated cannot lead to a steady state. Sinha and Wang have also shown that in fuel cells capillary forces dominate over viscous drag [32]. We will see below that in the current case the liquid water will not reach the inlet section because it evaporates. The predicted liquid phase pressure is around 5000 Pa, but this will change with the prescribed material properties. The capillary pressure is not defined inside the channels. We can see some liquid water predicted inside the channels but here the liquid phase pressure is identical to the gas phase pressure. A detailed channel model would account for a specified shear-off diameter of liquid droplets and a corresponding liquid pressure, but this is beyond the scope of the current work.

The predicted liquid saturation is shown in Fig. 6. Similar to previous calculations the maximum saturation is around 14%. However, in this case the irreducible saturation was assumed zero in this case for simplicity. The irreducible saturation has a dominant impact on the overall predicted saturation and consequently on the gas phase pressure drop across the cell, which means that the interdigitated design is well suited for multi-phase model validation.

Fig. 7 shows the predicted distribution of the oxygen concentration. Despite the fact that the stoichiometric flow ratio of 2.0 is fairly low and the current density is fairly high we see a relatively uniform distribution of oxygen at the catalyst layer, which is in contrast to the straight channel design. The inlet oxygen concentration in this and the following simulations is around 8.3 mole m^{-3}, but varies slightly with the inlet pressure. We also see that owing to diffusion the oxygen concentration decreases in the channel as well.

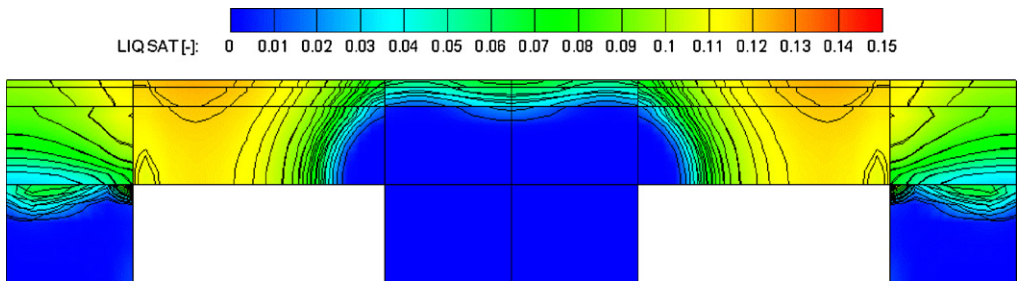

Fig. 6. Liquid saturation distribution for the base case investigated.

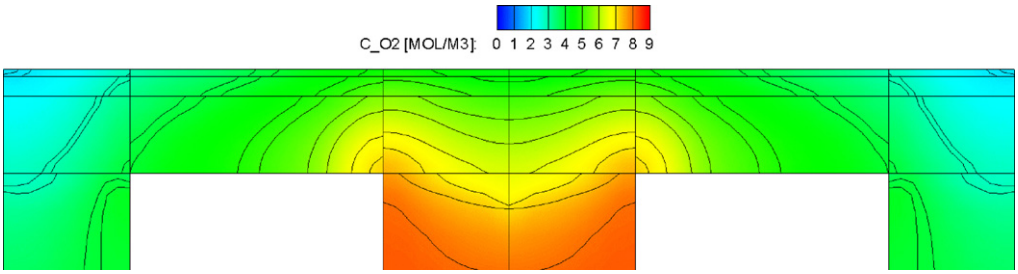

Fig. 7. Predicted oxygen concentration distribution for the base case investigated.

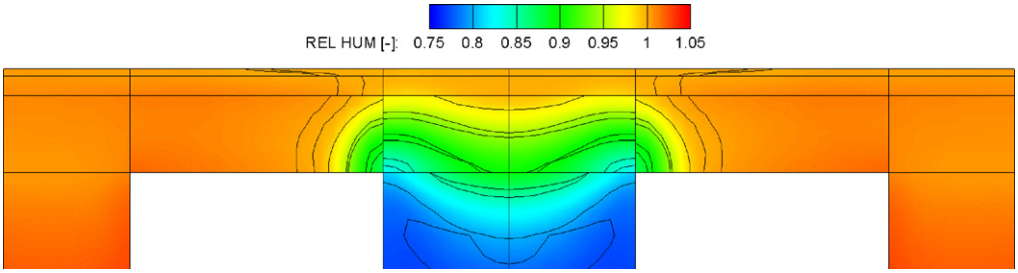

Fig. 8. Predicted relative humidity distribution for the base case investigated.

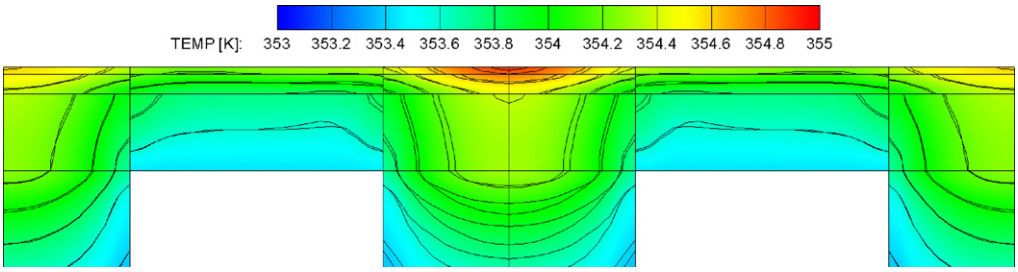

Fig. 9. Predicted temperature distribution for the base case investigated.

The relative humidity distribution is shown in Fig. 8. The RH increases from the inlet section to the under-land section where the multi-phase region starts. As was described by Berning and Djilali [18] this increase in RH is a direct consequence of the previously observed decrease in oxygen molar fraction. Once the multi-phase region is reached condensation is the predominant phase change mechanism. Overall the relative humidity remains relative constant here at around 100%. It is also interesting to see that the RH exceeds 100% at the bottom of the channel due to the specified temperature boundary condition where the coolant would be located. Hence a detailed channel model would need to account for condensation here.

The calculated temperature distribution is shown in Fig. 9. There is only a slight temperature increase predicted; its magnitude is determined by the thermal conductivity of the materials and the thermal contact resistances. It is typical that the highest temperature occurs under the channel region as heat is transferred from here to the land regions and the cooling channels which are here represented by a fixed temperature boundary. The temperature increase at the inlet section is higher than the temperature increase at the outlet section. This is caused by the fact that the local current density is coupled to the local oxygen concentration which is higher at the inlet section.

Finally, Fig. 10 shows the local rate of phase change. There are peak values for evaporation at the dry/wet interface as could be expected. It can also be seen that there is no direct correlation between the local rate of phase change and the temperature

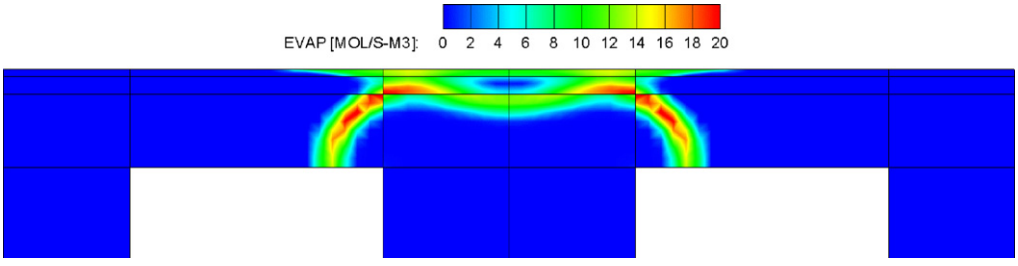

Fig. 10. Predicted rate of phase change for the base case investigated. Positive values indicate evaporation and negative values condensation.

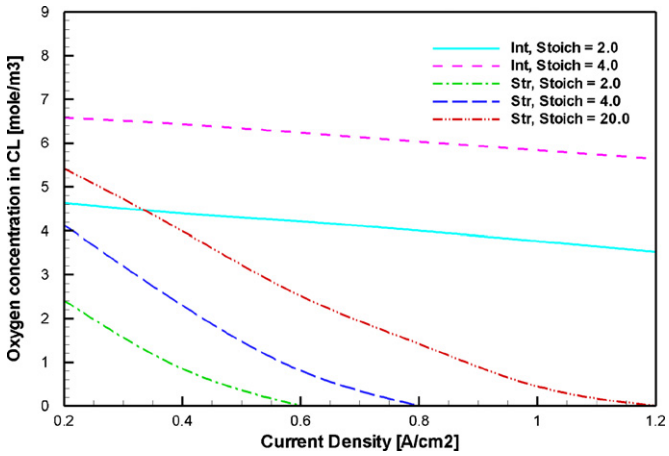

Fig. 11. Predicted average oxygen concentration inside the catalyst layer as function of current density for the interdigitated design (int.) and straight channel design (str.).

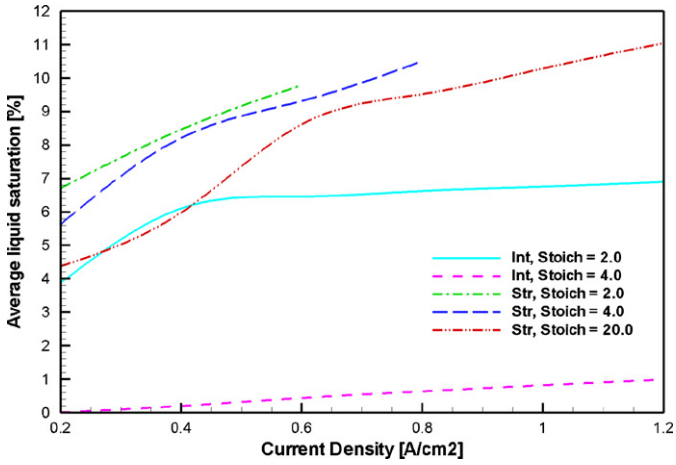

Fig. 12. Predicted average liquid saturation inside the porous layers as function of current density for the interdigitated design (int.) and straight channel design (str.).

distribution which is in agreement with the modeling predictions by Luo et al. [33].

4.2. Comparison between interdigitated and straight channel design

In order to sort out which flow field arrangement is preferable a comparison of straight channel design with the interdigitated design was performed using a similar geometrical set-up. Already here it becomes clear that a one-to-one comparison is not easily facilitated. The fact that the otherwise straight channels are subdivided between inlet section and outlet section means that we have only half the number of inlet channels in the interdigitated design which in turn means that the inlet velocity is twice as high compared to the straight channel set-up when keeping the same stoichiometric flow rate, and this makes a direct comparison difficult. The operating conditions and boundary conditions were the same as before, with the exception that the stoichiometric flow ratio was varied and the full range of current density explored, while prediction of the cell potential is obviously not a capability of the current model.

Fig. 11 shows the development of the average molar oxygen concentration inside the catalyst layer as function of current density. With the material parameters as chosen the predicted limiting current densities for the straight channel cases at stoichiometric flow ratios of 2.0 and 4.0 were relatively low at around 0.6 A cm^{-2} and 0.8 A cm^{-2}. This is why an additional case with a stoichiometric flow ratio of 20 was conducted which resulted in a predicted limiting current density of around 1.2 A cm^{-2}. By comparison the interdigitated case is not mass transfer controlled and the predicted oxygen concentration is higher compared to the straight channel set-up throughout all current densities. A modeling study performed by Bang suggested that oxygen starvation inside the catalyst layer can lead to local activation overpotentials as high as 700 mV [34], so the interdigitated design should lead to a better cell performance due to lower activation overpotential at high current densities. Moreover, the interdigitated design will allow for a wider land area and thus reduce the contact resistance at the cost of a slightly higher pressure drop. Thus two different mechanisms should enhance the cell performance when using the interdigitated design over the straight channel arrangement.

A further point that should be mentioned is that the down-the-channel concentration of oxygen in the inlet part should be higher for the interdigitated design, as nitrogen is also forced by convection through the porous media to the outlet side. Consequently there is a net flux of nitrogen from inlet section to outlet section which is absent in the straight channel set-up where there is no net flux of nitrogen due to the diffusive nature. All this means that towards the end of the inlet section of the interdigitated design the oxygen concentration should be significantly higher compared to the outlet section of the straight channel design which should lead to a smaller down-the-channel variation. This, however, has not been investigated in detail in the current work due to the quasi two-dimensional nature of this study.

Fig. 12 shows the average liquid saturation inside all the porous media as function of current density. Owing to the fact that the irreducible saturation was set to zero in these cases the values range up to 10% with peak values at 15%. The interdigitated design shows less water than the straight channel design, which is caused by the fact that the relatively dry inlet air of 75% RH is forced through the porous media. It can also be seen that at a stoichiometry of 4.0 there is a very small amount of liquid water. Not shown in the current plots is the predicted average relative humidity inside the catalyst layers. It is 100% for the straight channel design for the cases investigated. Employing the interdigitated design the dryer air is forced closer to the catalyst layer and the predicted average relative humidity for a stoichiometric flow ratio of 4 increases from 90.34% at a current density of 0.2 A cm^{-2} to a value of 94.6% at 1.2 A cm^{-2}, while it is above 99% in all cases for a stoichiometry of 2.0. It is very desirable to keep the catalyst layer fully humidified in order to reduce protonic losses here. In current fuel cells the catalyst layer thickness is roughly half that of the membrane which may range around 20–30 μm, but the electrolyte volume fraction in the CL is significantly lower which means that we may have high protonic losses if it is not properly humidified [34].

As liquid water management and removal is a major hurdle for fuel cell commercialization these days it is also of interest, how much of the product water leaves the cell in the gas phase and how much leaves the cell in the liquid phase. While it should be kept in mind that currently no phase change has been implemented in the channels the results presented here can still give an indication about the magnitude of the expected problems concerning liquid water removal. Fig. 13 summarizes the fraction of product water that leaves the cell in the vapour phase for the cases investigated. It is important to realize that even when most of the product water leaves the cell in the liquid phase this does not mean that there is no (stationary) liquid water inside the cell. This can be seen for the case of a straight channel and a stoichiometric flow ratio of 20, where up to a current density of 0.4 A cm^{-2} all the product water is predicted to leave the cell in the vapour phase but there is still

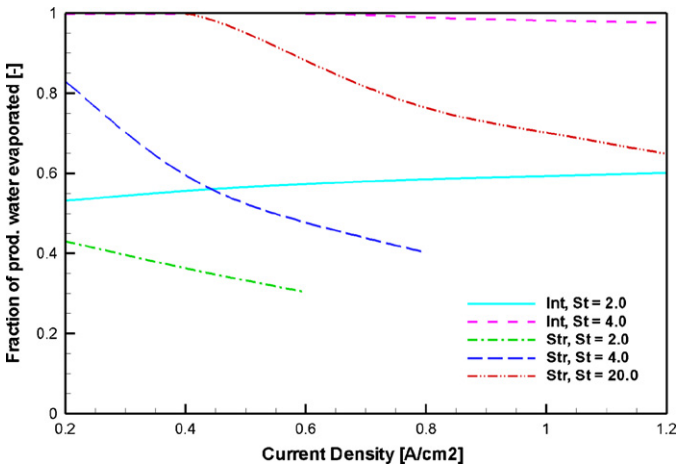

Fig. 13. Predicted fraction of product water evaporated as function of current density for the interdigitated design (int.) and straight channel design (str.).

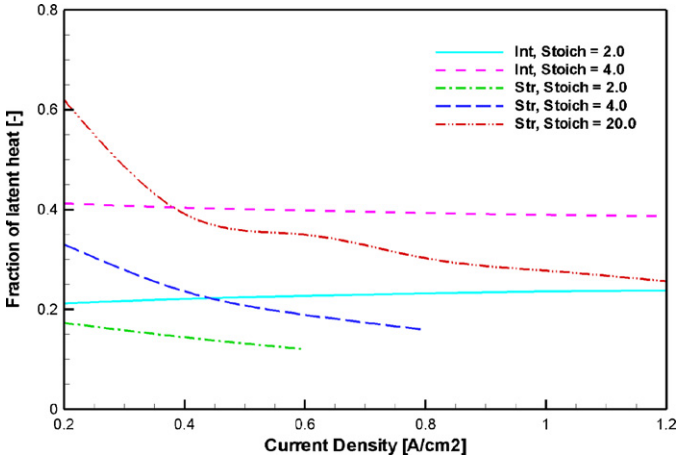

Fig. 14. Predicted fraction of latent heat on the total waste heat production as function of current density for the interdigitated design (int.) and straight channel design (str.).

stagnant water predicted inside the porous media. A comparison between the interdigitated design and the straight channel design shows also here that for similar operating conditions the interdigitated design is able to "shed off" a significantly higher fraction of the product water in the vapour phase, which means that the liquid water management may be significantly less problematic. In case of the interdigitated design the overall amount of evaporation will depend on the pressure drop across the land area. The RH, defined as $p_{g,\,H_2O}/p_{sat}(T)$, will decrease with a decreasing gas phase pressure which will lead to a stronger evaporation term [18]. This would make the in-plane permeability of the GDM a key parameter to control the evaporation rate: a low permeability leads to a high pressure drop and consequently a high fraction of product water will evaporate.

Table 2
Predicted pressure drop as function of current density for the interdigitated flow field.

Current density [A cm^{-2}]	0.2	0.4	0.6	0.8	1.0	1.2
Pressure drop Stoich 2 [Pa]	313	722	1095	1462	1822	2178
Pressure drop Stoich 4 [Pa]	510	1016	1521	2026	2531	3036

Another property of interest in these simulations is the fraction of waste heat that leaves the cell in the form of latent heat of evaporation, as the remaining fraction has to be picked up by the coolant and thus comes at the cost of a reduced system efficiency. Consequently the detailed heat balance incorporates the heat conducted out of the cell at the bipolar plate boundary, where the temperature has been fixed (*low y* interface). Fig. 14 shows that in the interdigitated design significantly less cooling is required compared to the straight channel design as more waste heat leaves the cell in the form of latent heat. Moreover, the percentage of latent heat remains fairly constant with current density which would facilitate an easier control of the coolant flow rate. A more detailed investigation of the effect of the cooling channel on the cell performance is to follow.

Finally, it was mentioned that the largest penalty for using the interdigitated design might be the increased pressure drop. Table 2 summarizes the predicted values as function of current density, which are as high as 3 kPa for the case of a stoichiometry of 4 and a current density of 1.2 A cm^{-2}. Again a reminder that despite the limited geometry investigated here the simulations should still yield a realistic pressure drop provided that the parameters for the relative permeability of the gas phase and the irreducible saturation are correct.

4.3. Specifying different material parameters

The final case presented here employs different material parameters in every domain in order to demonstrate the capabilities of the model. According to the Leverett equation employed here the capillary pressure is a function of permeability, porosity, contact angle and pore-size distribution inside the porous medium [35,36]. Moreover, the Leverett function is only employed to the reducible saturation [37,38], and in our model a different irreducible saturation can be specified in every layer [1]. This means that a change in either of the aforementioned properties leads automatically to a jump in the predicted saturation between the different layers, because the liquid phase pressure distribution has to be continuous [24]. The last case shown here can be compared with the first case investigated in detail in that the operating conditions were kept the same. However, the material properties were specified different in every layer. Inside the catalyst layer an irreducible saturation of 30% was applied due to the higher fraction of hydrophilic pores here. The in- and through-plane permeabilities were left unchanged at one Darcy, the porosity was at 75% and the contact angle (of the hydrophobic pores) was 120 degrees. The MPL had the same permeabilities and porosity, but the irreducible saturation was set to 10% due to the higher hydrophobicity. In the GDL an in-plane permeability of 5 Darcy was specified and the irreducible saturation was set to 20% the MPL. For the under-land section of the GDL the

Table 3
Final case material properties.

Parameter	Symbol	Unit	CL	MPL	GDL-land	GDL-channel
Porosity	ε	–	0.75	0.75	0.75	0.60
In-plane permeability	$K_{\parallel}$	m^2	1.0×10^{-12}	1.0×10^{-12}	5.0×10^{-12}	5.0×10^{-12}
Through-plane permeability	$K_{\perp}$	m^2	1.0×10^{-12}	1.0×10^{-12}	1.0×10^{-12}	1.0×10^{-12}
Contact angle	θ	°	120	120	120	120
Irreducible saturation	s_{irr}	–	0.30	0.10	0.20	0.20

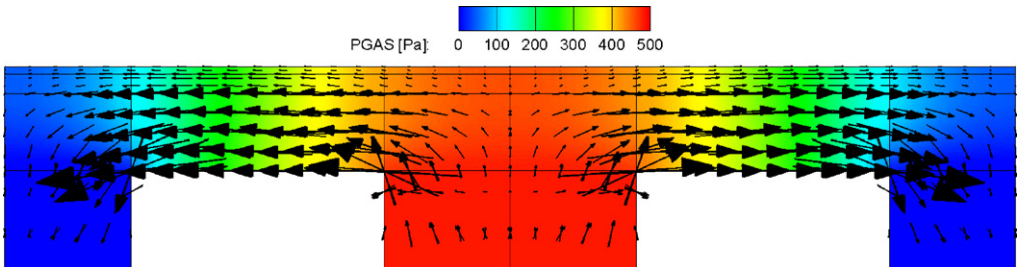

Fig. 15. Predicted gas phase pressure distribution and corresponding flow vectors for the last case investigated.

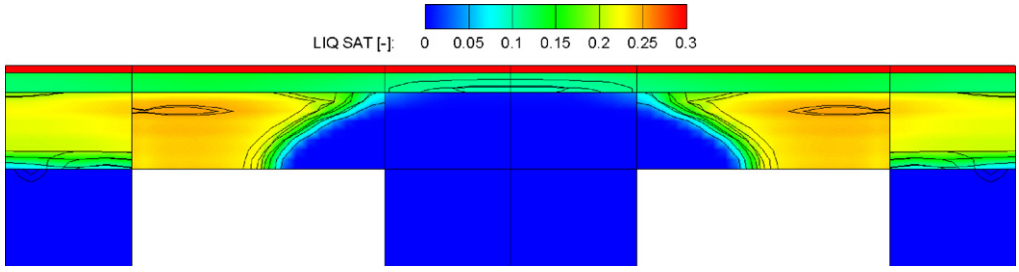

Fig. 16. Predicted liquid saturation distribution for the last case investigated.

porosity was reduced to 60% to account for the compression effect. It should be noted that by comparison the droplet size in the MPL is lower compared to the GDL, as it is calculated out of the characteristic pore size. This means that the surface area of the droplets is larger and hence by comparison the evaporation rate is higher in the MPL compared to the GDL for the same saturation level. We will see in the results that this effect apparently leads to a dryer GDL/MPL interface. Table 3 summarizes the material properties.

Starting at the calculated pressure distribution we see in Fig. 15 that due to the higher in-plane permeability the calculated pressure drop is now below 500 Pa. The flow vectors indicate that there is a much higher gas flux through the GDL substrate than through the MPL, again due to the higher in-plane permeability specified in this region. The predicted liquid water distribution is shown in Fig. 16. As was noticed before the specified irreducible saturation sets the level for the overall predicted saturation level. Inside the catalyst layer it is fairly constant ranging from 30% to 32.3% while inside the MPL it varies from 10% to 13.3% in the "wet" region. Under the channel the GDL interface with the MPL remains dry, which may be caused by the higher local evaporation rate in the MPL. The underland section of the GDL is predicted fairly wet at saturation levels above the specified capillary threshold of 20%. The jump condition between the land section and the channel section results out of the different porosities specified here, which leads to a higher predicted saturation level under the land section. The liquid phase pressure is depicted in Fig. 17 and shows that the maximum pre-

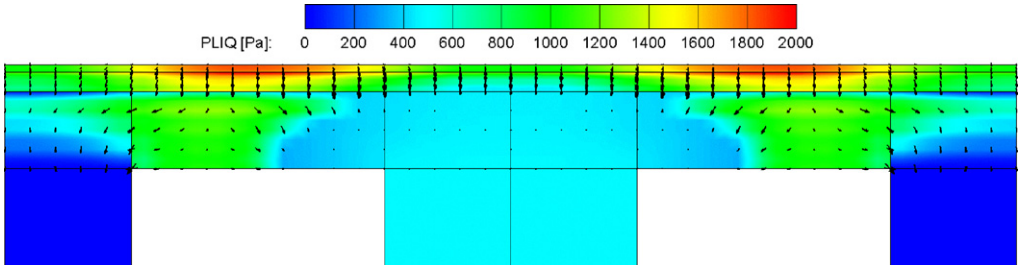

Fig. 17. Predicted liquid phase pressure distribution and corresponding flow vectors for the last case investigated.

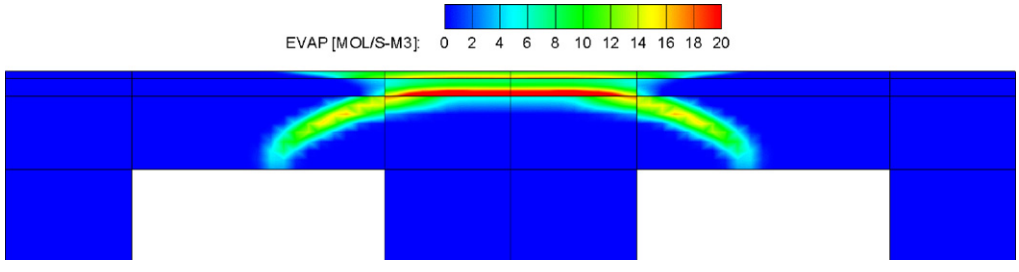

Fig. 18. Predicted rate of phase change distribution for the last case investigated.

dicted pressure is only at 2000 Pa and located inside the catalyst layer. Finally we see in Fig. 18 that the highest evaporation rate is at the interface between the MPL and the GDL under the channel section, which might cause the dry region here at the GDL side. This higher evaporation rate may be caused by two different effects: the Kelvin effect (see Eq. (11)) and the larger relative surface area due to the smaller pore size. A more detailed study on this is to follow.

5. Conclusions

A multi-phase model of the cathode side of a PEM fuel cell has been presented here. The model is based on the computational fluid dynamics package CFX-4.4 and utilizes the multi-fluid approach, which means that a complete set of transport equations has to be solved for every phase and detailed kinetics of phase change can be implemented. There is no inherent assumption that the gas phase relative humidity cannot exceed 100% and it is allowed that liquid water may co-exist with gas phase at less than 100% relative humidity. The model was applied to simulate the multi-phase flow inside a fuel cell with interdigitated flow field plates. The calculated pressure drop agrees well with experimental values reported in the literature. When the irreducible saturation was set to zero the predicted level of liquid saturation was at 15% similar to the straight channel design and the predicted oxygen concentration at the catalyst layer was fairly high and uniform. A comparative study was performed between the interdigitated design and a conventional straight channel set-up. It was found that by comparison the interdigitated cell yielded a higher and more uniform oxygen concentration at the catalyst layer, the overall liquid saturation was lower due to the enforced convection of relatively dry air. Moreover, less product water exits the porous media in the liquid phase which means that problems related to liquid water management are less severe. Finally, more of the waste heat is leaving the cell in the form of latent heat which leads to a lower load on the coolant. A final case showed the impact of employing different material parameters on the results and demonstrated the capabilities of the model. Coincidentally it was found that the higher evaporation rate caused by the Kelvin effect and the higher specific surface area in the MPL yields a lower liquid saturation in the GDL substrate. This effect will be investigated in more detail in the future.

Acknowledgements

This work was carried out under the Danish Energy Program, Grant # 33032-0145. TB would like to thank NW for helpful discussions and support.

References

[1] T. Berning, M. Odgaard, S. Kær, J. Electrochem. Soc. 156 (2009) B1301.
[2] T.V. Nguyen, J. Electrochem. Soc. 143 (1996) 103–105.
[3] J.S. Yi, T.V. Nguyen, J. Electrochem. Soc. 146 (1999) 38–45.
[4] W. He, G. Lin, T.V. Nguyen, AICHE J. 49 (2003) 3221–3228.
[5] L. Wang, H. Liu, J. Power Sources 134 (2004) 185–196.
[6] G. Hu, J. Fan, S. Chen, Y. Liu, K. Cen, J. Power Sources 136 (2004) 1–9.
[7] K.W. Lum, J.J. McGuirk, J. Electrochem. Soc. 152 (2005) A811–A817.
[8] H. Yamada, T. Hatanaka, H. Murata, Y. Morimoto, J. Electrochem. Soc. 153 (2006) A1748–A1754.
[9] W. Yan, C. Chen, S. Mei, C. Soong, F. Chen, J. Power Sources 162 (2006) 1157–1164.
[10] A.D. Le, B. Zhou, J. Power Sources 193 (2009) 665–683.
[11] L. Yu, G. Ren, M. Qin, X. Jiang, Ren. Energy 34 (2009) 530–543.
[12] T. Berning, N. Djilali, J. Power Sources 124 (2003) 440–452.
[13] L. Larminie, A. Dicks, Fuel Cell Systems Explained, 2nd ed., Wiley, 2003, p. 315.
[14] P.C. Sui, S. Kumar, N. Djilali, J. Power Sources 180 (2008) 410–422.
[15] S. Mazumder, J.V. Cole, J. Electrochem. Soc. 150 (2003) A1510–A1517.
[16] S. Mazumder, J.V. Cole, J. Electrochem. Soc. 150 (2003) A1503–A1509.
[17] Z.H. Wang, C.Y. Wang, K.S. Chen, J. Power Sources 94 (2001) 40–50.
[18] T. Berning, N. Djilali, J. Electrochem. Soc. 150 (2003) A1589–A1598.
[19] G. He, P. Ming, Z. Zhao, A. Abudula, Y. Xiao, J. Power Sources 163 (2007) 864–873.
[20] V. Gurau, T.A. Zawodzinski, J.A. Mann, J. Fuel Cell Sci. Technol. 5 (2008) 021009.
[21] C.Y. Wang, P. Cheng, Int. J. Heat Mass Transfer 39 (1996) 3607–3618.
[22] P. Cheng, C.Y. Wang, Int. J. Heat Mass Transfer 39 (1996) 3619–3632.
[23] T. Berning, D.M. Lu, N. Djilali, J. Power Sources 106 (2002) 284–294.
[24] J.H. Nam, M. Kaviany, Int. J. Heat Mass Transfer 46 (2003) 4595–4611.
[25] R.B. Bird, W.E. Steward, E.N. Lightfoot, Transport Phenomena, 2nd ed., Wiley, 2007, pp. 681–682.
[26] T.E. Springer, T.A. Zawodzinski, S. Gottesfeld, J. Electrochem. Soc. 138 (1991) 2334–2342.
[27] M. Eikerling, J. Electrochem. Soc. 153 (2006) E58–E70.
[28] T.R. Marrero, E.A. Mason, J. Phys. Chem. Ref. Data 1 (1972) 3–118.
[29] Y. Cengel, M.A. Boles, Thermodynamics – An Engineering Approach, 6th ed., McGraw Hill, 2007.
[30] M.J. Lampinen, M. Fomino, J. Electrochem. Soc. 140 (1993) 3537–3546.
[31] F.Y. Zhang, X.G. Yang, C.Y. Wang, J. Electrochem. Soc. 153 (2006) A225–A232.
[32] P.K. Sinha, C.Y. Wang, Electrochim. Acta 52 (2007) 7936–7945.
[33] G. Luo, H. Ju, C.Y. Wang, J. Electrochem. Soc. 154 (2007) B316–B321.
[34] M. Bang, Modeling of diffusive convective and electrochemical processes in PEM fuel cells, PhD Dissertation, Aalborg University, 2004.
[35] M.C. Leverett, Trans. AIME 142 (1976) 152.
[36] K.S. Udell, Int. J. Heat Mass Transfer 28 (1985) 485–495.
[37] D. Gerteisen, T. Heilmann, C. Ziegler, J. Power Sources 187 (2009) 165.
[38] H. Ju, J. Power Sources 185 (2008) 55–62.